Beyond hydrogen production

Solar−driven H_2S−donating value−added chemical production over $Mn_xCd_{1-x}S/Cd_yMn_{1-y}S$ catalyst

Dan, Meng; Xiang, Jianglai; Yang, Jian; Wu, Fan; Han, Chunqiu; Zhong, Yunqian; Zheng, Kaibo; Yu, Shan; Zhou, Ying

Published in:
Applied Catalysis B: Environmental

Link to article, DOI:
10.1016/j.apcatb.2020.119706

Publication date:
2021

Document Version
Peer reviewed version

Beyond Hydrogen Production: Solar-Driven H_2S-Donating Value-Added Chemical Production over $Mn_xCd_{1-x}S/Cd_yMn_{1-y}S$ Catalyst

Meng Dan[a, b, c, #], Jianglai Xiang[a, b, #], Jian Yang[b], Fan Wu[b], Chunqiu Han[a, b,] Yunqian Zhong[a, b,], Kaibo Zheng[c,d], Shan Yu[b], Ying Zhou[a, b,*]

a State Key Laboratory of Oil and Gas Reservoir Geology and Exploitation, Southwest Petroleum University, Chengdu 610500, China.

b The Center of New Energy Materials and Technology, School of Materials Science and Engineering, Southwest Petroleum University, Chengdu 610500, China.

c Department of Chemical Physics and NanoLund, Lund University, Box 124, 22100, Lund, Sweden.

d Department of Chemistry, Technical University of Denmark, DK-2800 Kongens Lyngby, Denmark.

* Correspondence author:

Email: yzhou@swpu.edu.cn; Fax: +86 28 83037406; Tel: +86 28 83037411

# These authors contributed equally to this work.

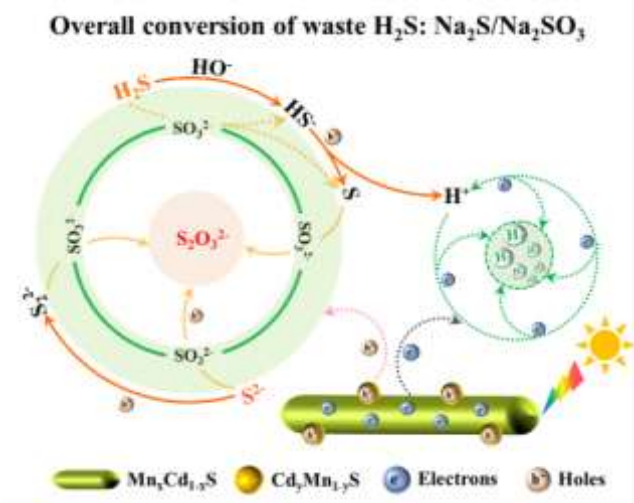

This work proposes a smart H_2S-induced product-targeting (HIPT) strategy for the conversion of Na_2S/Na_2SO_3 into value-added chemicals coupled with H_2 evolution with state-of-the-art efficiency via overall H_2S splitting over a "Dual-Solid-Solution" heterostructure.

Highlights

- A novel H_2S-induced product-targeting strategy is developed, which integrated solar-driven Na_2S/Na_2SO_3 conversion with overall H_2S splitting.
- An important industrial sulfur product $Na_2S_2O_3$ is obtained with high selectivity (almost 100%) and conversion (99%).
- A state-of-the-art H_2 evolution rate as high as 113 mmol g^{-1} h^{-1} (AQE = 77%, 440 nm) is achieved.
- An advanced method is provided on the design of high efficiency "Dual-Solid-Solution" heterojunction systems.

Abstract

Simultaneous hydrogen (H_2) evolution and value-added chemicals production are highly attractive but have not drawn enough attention. Here, we demonstrate a hydrogen sulphide (H_2S)-induced product-targeting (HIPT) strategy for the coproduction of H_2 and valuable chemical feedstocks from Na_2S/Na_2SO_3 via overall H_2S splitting using a $Mn_xCd_{1-x}S/Cd_yMn_{1-y}S$ catalyst driven by visible light excitation. With this chemistry, 113 mmol g^{-1} h^{-1} of hydrogen evolution rate is achieved, surpassing most of the previously reported state-of-the-art photocatalyst, together with the production of value-added $Na_2S_2O_3$ with nearly 100% selectivity. This work not only provides a good example for solar energy conversion via overall H_2S splitting, but also offers new insights into the resource utilization of sacrificial donor (Na_2S/Na_2SO_3) in various catalytic fields such as H_2O splitting and CO_2 reduction.

Keywords: sacrificial reagent conversion, overall H_2S splitting, hydrogen evolution, value-added chemical, "Dual-Solid-Solution" heterostructure

1. Introduction

Solar energy is widely regarded as a free, inexhaustible and renewable source of clean energy, and the sunlight reaching the Earth's surface on an hourly basis actually exceeds the annual global energy consumption.[1-2] However, there is always the issue of the intermittency of solar power utilization.[3-4] The production of H_2 via sunlight-driven photocatalytic process represents a promising strategy to harvest solar energy.[5-7] In this process, photoinduced electrons are applied to reduce protons from hydrogen

sources (eg. H_2O, H_2S, etc.), triggering predominant conversion from solar energy to hydrogen energy.[8-10] Nevertheless, this process also generates holes that, if not involved in oxidizing the substrate, is inclined to oxidize the photocatalyst itself, resulting in diminishing solar to hydrogen energy transformation efficiency and photocorrosion of the photocatalyst.[11-12] In general, the holes can be intercepted efficiently by a sacrificial electron donor, which enables to accelerate the hydrogen evolution rate and extend the life cycle of the catalyst.[13-14] However, such processes produce undesirable by-products, and more importantly, the depletion of energy required to produce the sacrificial reagents cannot be offset by the energy harvesting from hydrogen generation.[15-16] The employment of sacrificial reagents that are produced from renewable and abundant raw materials is therefore of vital importance, and it is also necessary for them to be easily oxidized to produce value-added chemicals.

In this scenario, Na_2S/Na_2SO_3 has attracted much attention thanks to its excellent electron-donating ability and abundance of resource.[17-18] So far the highest solar-to-H_2 apparent quantum efficiency of up to ~93% at 420 nm is achieved using Na_2S/Na_2SO_3 as the holes scavenger.[19] Furthermore, the carbon-neutrality of Na_2S/Na_2SO_3 in contrast to other organic sacrificial reagents (eg. alcohols (methanol, ethanol, ethylene glycol, glycerol), lactic acid and etc.) is more attractive as building blocks for sustanble energy solution.[20--22] More importantly, Na_2S/Na_2SO_3 oxidation during the photocatalytic reaction great potential to produce $Na_2S_2O_3$, a valuable product widely used as fixing agent, reducing agent and bleaching agent, etc., in the industrial activities,[23--30] which is thus highly desirable to achieve simultaneous H_2

evolution with value-added chemical production. However, besides $Na_2S_2O_3$, other unexpeceted over-oxidative sulfur species (SO_4^{2-}, $S_2O_6^{2-}$) can also be generated in the process of Na_2S/Na_2SO_3 oxidation especially on the basic condition,[30-32] which remains a barrier for the extraction of $Na_2S_2O_3$ to realize the resource utilization of Na_2S/Na_2SO_3.

Herein, we present a H_2S-induced product-targeting (HIPT) strategy under visible light irradiation to tackle this issue. As shown in **Scheme 1,** the introduction of acidic H_2S molecules favors to turn the baseic Na_2S/Na_2SO_3 solution to a near-neutral condition so as to efficiently acquire $S_2O_3^{2-}$ and substantially prevent over-oxidative sulfur species (SO_4^{2-}, $S_2O_6^{2-}$) production (Equations 1, 2, 3, 5, 6).[33-34] Meanwhile, $Na_2S_2O_3$ is expected to be the sole production of sulphur species after the photocatalytic process because Na_2SO_3 can be completely consumed by adequate H_2S to form $Na_2S_2O_3$ (Equations 4,5). This was indeed verified by Fourier transform infrared (FTIR) spectroscopy and Ion Chromatography (IC). Besides, the state-of-the-art performance for photocatalytic H_2 production (113 mmol g^{-1} h^{-1}) from H_2S is realized by using a "Dual-Solid-Solution" metal sulphide heterostructure as the photocatalyst. To the best of our knowledge, this is the first report on the conversion of Na_2S/Na_2SO_3 into value-added chemicals coupled with robust H_2 evolution via overall H_2S splitting. It provides a reliable avenue for the resource utilization of sacrificial donor in various catalytic reactions.

Scheme 1. Illustration of overall conversion of H_2S and Na_2S/Na_2SO_3 over novel $Mn_xCd_{1-x}S/Cd_yMn_{1-y}S$ "Dual-Solid-Solution" Z-scheme hybrids.

$$HS^- + 2h^+_{VB} \rightarrow H^+ + S^0 \quad (1)$$

$$2S^{2-} + 2h^+_{VB} \rightarrow S_2^{2-} \quad (2)$$

$$SO_3^{2-} + S^{2-} + 2h^+_{VB} \rightarrow S_2O_3^{2-} \quad (3)$$

$$SO_3^{2-} + 4H_2S \rightarrow 2HS^- + 3S + 3H_2O \quad (4)$$

$$S + SO_3^{2-} \rightarrow S_2O_3^{2-} \quad (5)$$

$$SO_3^{2-} + S_2^{2-} \rightarrow S_2O_3^{2-} + S^{2-} \quad (6)$$

2. Experimental section

2.1 Synthesis of $Mn_xCd_{1-x}S/Cd_yMn_{1-y}S$ (MC) composites

The composites were synthesized by a solvothermal method. In a typical procedure, x mmol $CdCl_2 \cdot 2.5H_2O$, 2-x mmol $Mn(CH_3COO)_2 \cdot 4H_2O$ and 9 mmol thioacetamide (TAA) were dissolved into 25 mL pyridine solution. The MnS/CdS composites were denoted as MC-y (y =1, 2, 3, 4 ,5), meaning the molar ratio of y were 10%, 20%, 30%,

40%, 50% in total 2 mmol precursors (of total Mn and Cd sources), respectively. The obtained homogeneous solution was transferred to a 50 mL Teflon-lined stainless-steel autoclave for maintaining 18 h under 180 ℃. After cooling to room temperature naturally, the suspension was centrifuged and washed several times with ultrapure water and ethanol. And then the collected precipitates were dried at 60 ℃ overnight in a vacuum oven. MnS and CdS were prepared through the same procedures without adding Cd or Mn sources.

2.2 Characterization

The structure and crystallinity of samples were investigated by the X-ray diffraction (XRD, PANalytical X'pert with Cu Kα radiation). To obtain the surface chemical composition and binding environment of the samples, the X-ray photoelectron spectroscopy (XPS, Thermo ESCALAB250Xi) measurements were performed referencing to the C 1 s level at 284.8 eV. The the TEM, high resolution TEM (HRTEM) and the corresponding EDX elemental mapping were conducted to gain the mophology , microstructure and compositions of samples. The N_2 adsorption-desorption isotherm and pore-size distributions were determined by the nitrogen adsorption method (Quadrasorb SI), the specific area of the samples was calculated using the Brunauer-Emmett Teller (BET) method. Inductively coupled plasma atomic emission spectrometry (ICP-AES, Varian ES) was used to identify the compositions of the samples. The UV-visible diffuse reflectance spectrum (UV-vis DRS, Shimadzu UV-2600 with an tntegratting spere) of the samples were recorded at room temperature

using $BaSO_4$ as the reflectance standard. The surface photovoltage (SPV) spectra were obtained by a TLS-SPV530 spectrometer (Zolix Instruments Co., Beijing). The contact angles were tested with a OCA25 video optical contact angle tester (Data Physics, Germany).

2.3 Photocatalytic H_2 evolution performance evaluations

The photocatalytic reaction was conducted in a 50 mL home-made photoreactor (Pyrex-flask). Firstly, 1.5 mg photocatalyst was introduced as suspension into 50 mL 0.1/1.5 M of Na_2S/Na_2SO_3 mixed solution after ultrasonication for 30 min. Secondly, the reactor was de-aerated with Ar for 10 min followed by bubbling 0.15 mol H_2S gas into the abovementioned solution for 3 h. Thirdly, the photoreactor was irradiated by a 300 Xenon lamp with UV cutoff filter ($\lambda > 420$ nm). The amount of evolved H_2 was monitored by Shimadzu GC 2010 Plus equipped with a TCD detector, using 5 Å molecular sieve and Ar as the carrier gas. The H_2 evolution rates were calculated based on H_2 amount generated within the first 5 h of reaction.

2.4 Photocatalytic oxidation products investigations

The oxidation products were firstly systematically investigated by coupling the Infrared spectrometer (Bruker, Tensor II) and ion chromatograph (930 Compact IC Flex, Metrohm, Switzerland). Concretely, after the reaction, the solution was centrifugated under 1000 r/min for 10 min, and then 10-20 μL of the supernatant was drop-cast on KBr before pressed into pellets and conducting FT-IR test. The photocatalytic oxidation products were further determined by the IC technique. 1 μL solution after the reaction

was added to 10 mL water, and then the as-obtained solution was injected into the ion chromatograph. Notably, all the tested solutions were mixed and collected after three times experiments.

2.5 The apparent quantum efficiency (AQE)

The AQE was calculated according to Eq. (7). The number of produced H_2 molecules was measured by GC (Shimadzu GC-2010 Plus) and the number of incident photons was determined from the output of a monochromatic LED lamp.

$$\mathrm{AQY} = \frac{\text{number of reacted electrons}}{\text{number of incident photons}} \times 100\%$$

$$= \frac{2 \times \text{number of evolved hydrogen molecules}}{\text{number of incident photons}} \times 100\% \qquad (7)$$

2.6 Photoeletrochemical measurements

The Electro-chemical impedance spectroscopy (EIS), Linear sweep voltammetry (LSV), Transient photocurrent response and Mott-Schottky curve were investigated with CHI660E workstation by using Pt wire as a counter, and saturated calomel electrode as reference electrode. The working electrode with an active area of ca. 1 cm^2 was prepared by a doctor blading technique (ITO, film thickness: 50 μm). The 1.2 M Na_2SO_3 was used as electrolyte. The EIS and Transient photocurrent response over all the samples at open circuit potential were investigated under visible-light irradiation ($\lambda > 420$ nm). LSV was conducted at a scan rate of 10 mV/s. The Mott-Schottky curves were collected at a fixed frequency of 500 and 700 Hz.

2.7 Density functional theory DFT calculation

The DFT calculations were carried out using the generalized gradient approximation (GGA) exchange-correlation functional of the Perdew-Burke-Ernzerh of (PBE) type as implemented in the Cambridge Sequential Total Energy Package (CASTEP). [35-36] The cutoff energy of the plane-wave expansion was set to 400 eV. The Brillouin zone was elected with 2×2×1 Monkhorst-Pack k-point grids for the structure optimizations. All geometries were adequately optimized until the convergence criteria of energy and force reached 1×10^{-5} eV and 0.02 eV/Å, respectively. The neighboring system interference along the c axis was avoided by building a vacuum space of 20 Å. The first-principles DFT simulation was carried out based on constructed crystal structures of the CdS (001) surfaces.

3. Results and Discussion

3.1 Photocatalytic performance evaluations

First, the photocatalytic overall H_2S splitting using $Mn_xCd_{1-x}S/Cd_yMn_{1-y}S$ (MC) as the catalysts was investigated in the Na_2S/Na_2SO_3 solution under visible-light irradiation ($\lambda > 420$ nm). Here, the samples obtained using a simple solvothermal route at 180 ℃ for 18 h with different $CdCl_2$ dosages are denoted as MC-y (y=1, 2, 3, 4, 5) (See Experimental Section for more detailed information). The blank experiments revealed that H_2 was not found in the absence of photocatalyst or light irradiation. 1.5 M Na_2SO_3 and 0.1 M Na_2S are applied to deliver an optimal hydrogen evolution rate (**Fig. 1a**). **Fig. 1b** and **Fig. S1a** show that all the MC composites exhibit superior H_2

evolution performance as compared to the pristine MnS and CdS. A maximum H_2 production rate of 113 mmol g^{-1} h^{-1} can be achieved, which is ~170 and 24 times higher than that of MnS and CdS, respectively (**Fig. 1b**), outperforming most of the reported state-of-the-art photocatalysts (**Table S1**). The corresponding apparent quantum efficiency (AQE) of MC-3 is as high as 77% at 440 nm. More importantly, the AQE complies with the UV-vis diffuse reflectance spectra (UV-vis DRS) of MC-3, confirming the photocatalytic nature of H_2 production over MC hybrids (**Fig. S1b**). The X-ray photoelectron spectroscopy (XPS) analysis of MC-3 before and after the reaction corroborates the excellent photostability of the present system (**Fig. S2**).

Despite extensive efforts, the development of photocatalytic H_2S splitting systems simultaneously possessing superior H_2 evolution performance and high selectivity for value-added oxidation product is still in its infancy, as several issues urgently need to be addressed. First, surface sites are susceptible to be occupied by solid S and visible light absorption shielded by the colored S_2^{2-}, [33-34,37-39] hindering the long-term stability and activity of the photocatalysts. Second, the other sulfur species such as $S_2O_6^{2-}$ and SO_4^{2-} are detrimental environmental effect and impedes recyclable utilization of oxidation products. [33-34,37-39] Above all, the highly selective production of value-added sulfur species is important but not eventually achievable due to the competitive generation of S, S_2^{2-}, $S_2O_6^{2-}$, SO_4^{2-}. Therefore, it is imperative to get an in-depth insight into oxidation process of H_2S splitting, which could guide us to the landscape for establishing photocatalytic H_2S splitting system with high activity and selectivity.

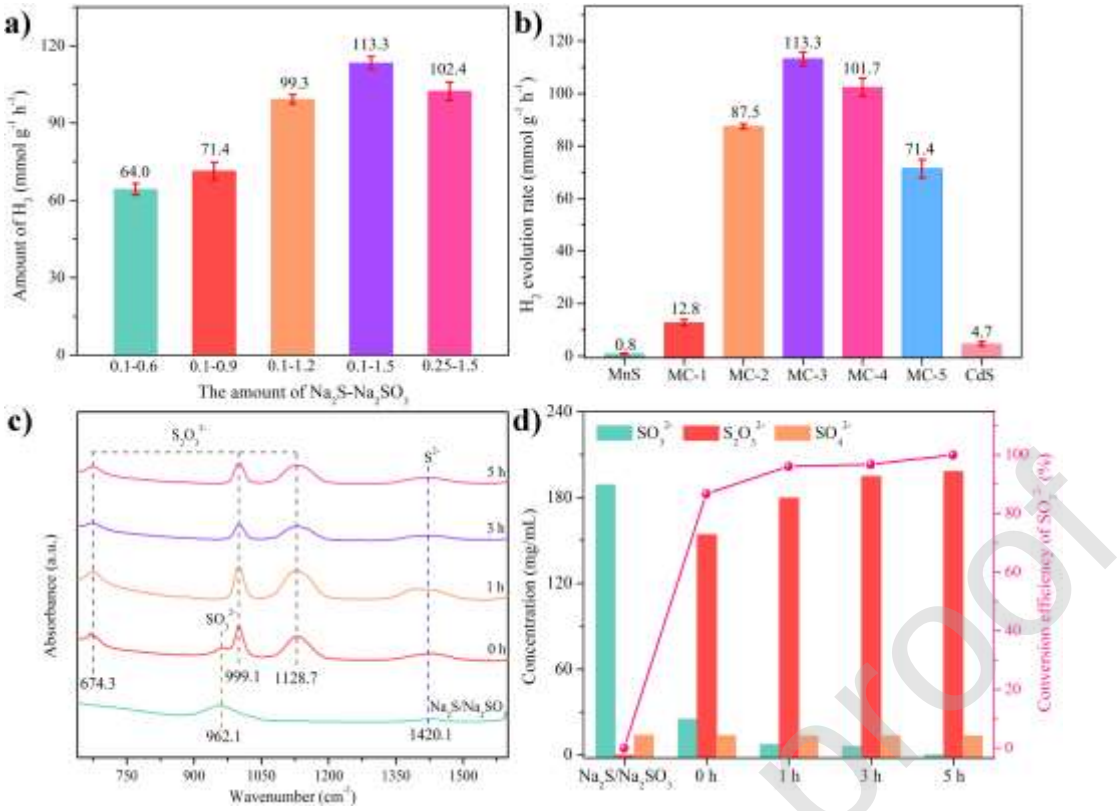

Fig. 1. a) Relation of the concentration of reaction media to the hydrogen evolution rate, b) Photocatalytic H_2 production from waste H_2S over all tested samples under visible light irradiation ($\lambda > 420$ nm), c) FTIR spectra, d) IC analysis of ions in the reaction solution with the presence of MC-3 sample.

In this work, the H_2S oxidation process is systematically investigated using FTIR technique in combination with IC and XRD over MC-3 photocatalyst in the Na_2S/Na_2SO_3 solution (**Fig. 1c, d** and **Fig. S3**), which could guide us to the landscape for establishing photocatalytic H_2S splitting system with high activity and selectivity. The FTIR spectra reveal only the presence of S^{2-} (1420.1 cm^{-1}) and SO_3^{2-} (962.1 cm^{-1}) prior to H_2S addition, [40-41] suggesting the absence of chemical reaction between Na_2S and Na_2SO_3. Nevertheless, peaks at 674.3, 999.1, 1128.7 cm^{-1} feature that the conversion of SO_3^{2-} to $S_2O_3^{2-}$ ion under H_2S-assisted acidic conditions (Equations 4,5)

can be detected upon the introduction of H_2S gas.[42] Moreover, $S_2O_3^{2-}$ species are the only products as a result of the almost consumption of SO_3^{2-} with irradiation for 1h or even longer (**Scheme 1**, Equations 3, 5, 6). To render further insights into the oxidation process of H_2S splitting, IC measurements were performed, as shown in **Fig. 1d**. Before irradiation, plenty of SO_3^{2-} ions (~86.7%) can be chemically converted into $S_2O_3^{2-}$, which is consistent with the FTIR analysis. More importantly, the molar ratio of depleted SO_3^{2-} to the resulting $S_2O_3^{2-}$ is 4:3, which corresponds to the Equations 4, 5. This validates the present HIPT strategy. After 1h of illumination, ~96.1% SO_3^{2-} ions are depleted. It's noted that expanding the irradiation time more than 3 h can lead to a removal efficiency of approximate 99.9% for SO_3^{2-}. The above results quantitatively elaborate the anticipated overall conversion of Na_2S/Na_2SO_3 into value-added $Na_2S_2O_3$, as further confirmed by corresponding XRD test (JCPDS 25-0680) (**Fig. S3**). These results clearly revealed the photo-driven conversion of H_2S with high activity and selectivity over MC sample in Na_2S/Na_2SO_3 solution.

To further reveal the resource conversion process of waste H_2S, a series of comparative experiments were conducted. First, the photocatalytic oxidation process of Na_2S/Na_2SO_3 over MC-3 in the absence of H_2S was investigated by FTIR test. As seen in **Fig. 2a**, the complex oxidation products (SO_4^{2-}, $S_2O_3^{2-}$, $S_2O_6^{2-}$) can be simultaneously detected in the absence of H_2S. Meantime, the excess SO_3^{2-} from reaction medium was also observed.[41,42] The various S-containing species in reaction solution seriously impedes recyclable utilization of oxidation products in the absence of H_2S. This result demonstrates that the presence of H_2S can directionally induce the formation of

photocatalytic-oxidative product $S_2O_3^{2-}$. Then, the amount of H_2S to the effect of reaction process was also investigated and studied based on the FTIR test (**Fig. 2b**). The complex oxidation products (SO_4^{2-}, $S_2O_3^{2-}$, $S_2O_6^{2-}$) can be simultaneously detected after irradiation for 5h when the amount of H_2S is equal to 25 mmol (25-H_2S).[41, 42] Interestingly, the complexity of oxidation products is found to be closely related with the amount of H_2S, for which the obviously descend complexity with increased H_2S content. When the amount of H_2S is given as 75 mmol (75-H_2S), the sulfur-containing oxidation products mainly refer to the $S_2O_3^{2-}$, but the excess SO_3^{2-} from reaction medium can also be observed. With further increasing the amount of H_2S (150 mmol, using 150-150 mL 0.1-1.5 M HCl-Na_2S solution), all of the SO_3^{2-} are converted into $S_2O_3^{2-}$ (**Fig 1c**), which can be attributed to the introduction of acidic H_2S molecules turning the basic Na_2S/Na_2SO_3 solution to a near-neutral condition so as to efficiently obtain $S_2O_3^{2-}$ and substantially prevent other oxidation products (SO_4^{2-}, $S_2O_6^{2-}$). Meanwhile, the H_2 evolution performance also exhibits a significant increase with increasing the amount of H_2S (**Fig. S4**). However, the existence of H_2S can impact the pH value of the reaction solution. So, a comparative experiment was also performed by replacing H_2S with HCl and the pH was maintained within the range of 7.5-8.0 to further exclude the influence of pH values.[34] Notably, no photocatalytic H_2 production was observed when the pH value was modulated by using the HCl. These results can further authenticate the rationality of the HIPT strategy for overall resource utilization of waste H_2S.

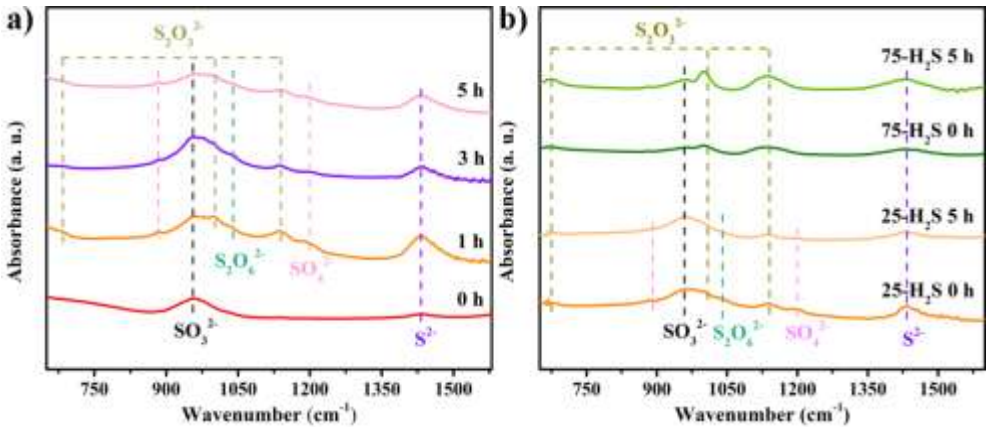

Fig. 2. a) FTIR spectra of the reaction process in the absence of H_2S; b) FTIR result with difference concentrations of H_2S using MC-3 as catalyst (The content of H_2S can be controlled by modulating the volume of 1-2 M HCl-Na_2S solution (25-25 and 75-75 mL)). **Conditions:** reaction medium, 0.1-1.5 M Na_2S-Na_2SO_3; catalyst: 1.5 mg; light source, 300 W Xe lamp (λ > 420 nm))

3.2 Structure, composition and morphology

For a photocatalytic process, the photocatalyst is pivotal to the superior conversion efficiency. Therefore, various characterization technologies were carried out to explore the structure-performance relationship. As shown in **Fig. S5**, the cubic MnS (JCPDS 06-0518) and hexagonal CdS (JCPDS 65-3413) can be indexed either in the absence of Cd or Mn precursor. For all the samples fabricated in the presence of both Cd and Mn precursors, the hexagonal CdS (JCPDS 65-3413) and hexagonal MnS (JCPDS 41-1049) phases can be simultaneously observed. Interestingly, as the Cd content increased, the diffraction peaks of MnS and CdS phases in the MC composites shifted obviously toward lower or higher angles, indicating the formation of the $Mn_xCd_{1-x}S$ and $Cd_yMn_{1-y}S$ solid solutions. The compositions of all MC samples were identified by the inductively coupled plasma atomic emission spectrometry (ICP-AES) elemental

analysis (**Table S2**).

XPS analysis was conducted to verify the surface chemical states of MC hybrids (**Fig. 3a, b** and **Fig. S6**). XPS survey spectra show the coexistence of Mn, Cd, and S (**Fig. S6a**). Compared with those of MnS and CdS, the binding energies of Mn 2p and Cd 3d of MC-3 are red-shifted by ~ 1 and 0.3 eV, respectively (**Fig. 3a, b).** In the S 2p high-resolution spectra, two deconvoluted peaks at 161.3 and 162.4 eV (**Fig. S6b**) can be assigned to S^{2-}, [43-44] larger than that of MnS but smaller than CdS. These results reveal a strong interaction for $Mn_xCd_{1-x}S$ and $Cd_yMn_{1-y}S$ solid solutions, [45-46] which may be attributed to the formation of heterostructure between $Mn_xCd_{1-x}S$ and $Cd_yMn_{1-y}S$ solid solutions. The XPS valence band spectra reflect a higher level of valence band maximum (VBM) for MC-3 (1.0 eV) in comparison with that of MnS (1.2 eV) and CdS (1.7 eV), which is favorable for $Na_2S_2O_3$ production and for inhibiting the formation of over-oxidized products ($S_2O_6^{2-}$ and SO_4^{2-}) (**Fig. S6c**).

Transmission electron microscopy (TEM) images show that MC-3 sample is composed of nanorods and nanoparticles with intimate contact (**Fig. 3c, d**). Such conjunction may contribute to the slightly enhanced Brunauer-Emmett-Teller (BET) surface area (9.4 $m^2 g^{-1}$) for MC-3 composite as compared to the pristine MnS (3.6 $m^2 g^{-1}$) and CdS (6.8 $m^2 g^{-1}$) (**Fig. S7** and **Table S3**). The clear lattice fringes with spacing of 0.35 and 0.21 nm are assigned to (100) of $Mn_xCd_{1-x}S$ (MnS phase) nanorod and (110) of $Cd_yMn_{1-y}S$ (CdS phase) nanoparticle, respectively (**Fig. 3e)**. The Energy-dispersive X-ray spectroscopy (EDS) elemental mapping images confirm the successful fabrication of "Dual-Solid-Solution" heterostructure with close interface interaction

(**Fig. 3f**) and the corresponding composition can be expressed as $Mn_{0.74}Cd_{0.28}S/Cd_{0.78}Mn_{0.24}S$ from the EDS elemental analysis (**Fig. S8**). As we know, the "Solid solution-Heterojunction" system meets the prerequisites required for an efficient photocatalytic process due to the superiority in light-harvesting-efficiency, carriers mobility and surface reaction dynamics.

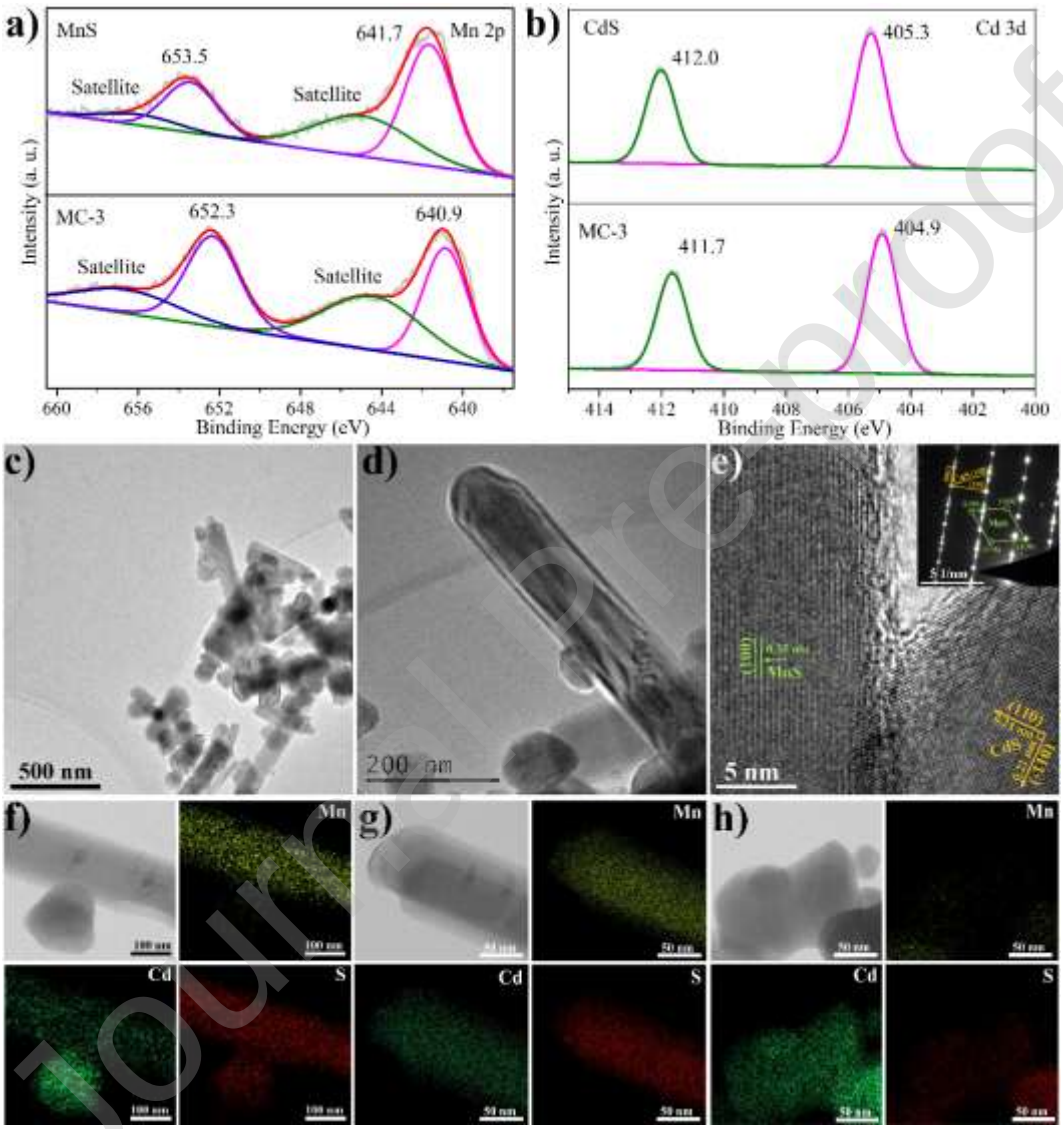

Fig. 3. a) Mn 2p, b) Cd 3d XPS spectra of the MnS, MC-3 and CdS samples, c) Low- and d) high-magnification TEM images, e) HRTEM image with inset of corresponding SAED pattern, EDX elemental mapping on f) nanorod/nanoparticle g) nanorod and h) nanoparticle of the MI-3 sample.

3.3 Band structure investigations

And then, a combined analysis of the UV-Vis DRS spectrum and Mott–Schottky (MS) plots was adopted to examine the electronic band alignment of MC-3 heterostructure (**Fig. 4a**). The UV-Vis DRS spectrum of the MC-3 composite presents typical features of individual $Mn_xCd_{1-x}S$ and $Cd_yMn_{1-y}S$ with respect band gap of 2.86 and 2.40 eV. The Mott–Schottky plots reveal p-type characteristic of both $Mn_xCd_{1-x}S$ and $Cd_yMn_{1-y}S$ owing to the negative slope of the linear plots at 0.77 and 1.01 V vs. NHE, [47-48] which is accordant with the flat-band potential values (E_{fb}) of $Mn_xCd_{1-x}S$ and $Cd_yMn_{1-y}S$, respectively. The VBM position (E_{VBM}) for $Mn_xCd_{1-x}S$ and $Cd_yMn_{1-y}S$ can be further estimated as 0.87 and 1.11 V, respectively, considering that E_{fb} is about 0.1 V more positive than the VB position.[49] Correspondingly, the conduction band minimum (CBM) potential (E_{CBM}) is obtained at -1.99 and -1.29 V, respectively. Hence, the energy band alignment can be depicted as shown in **Fig. 4b**. We further applied DFT calculations to refine the electronic structures of heterostructure. In the charge transport analysis, the work function is higher for $Cd_yMn_{1-y}S$ and lower in the $Mn_xCd_{1-x}S$ (**Fig. 4c, d**), which allows built-in electric field to be directed from $Mn_xCd_{1-x}S$ to $Cd_yMn_{1-y}S$.[50] Base on the above characterization we can conclude a direct Z-scheme type heterojunction between $Mn_xCd_{1-x}S$ and $Cd_yMn_{1-y}S$ (**Fig. 4b**). In general, the direct Z-scheme heterostructure is an ideal system for photocatalytic reaction given that the remarkable spatial separation and more energetic redox ability of photoinduced charges can be simultaneously remained. Concretely, when MC samples are excited, the photoinduced electrons in $Cd_yMn_{1-y}S$ and photoinduced holes in $Mn_xCd_{1-x}S$ would

preferentially migrate to the heterojunction interface and recombine with each other due to the existence of internal electric field pointing from $Cd_yMn_{1-y}S$ to $Mn_xCd_{1-x}S$.

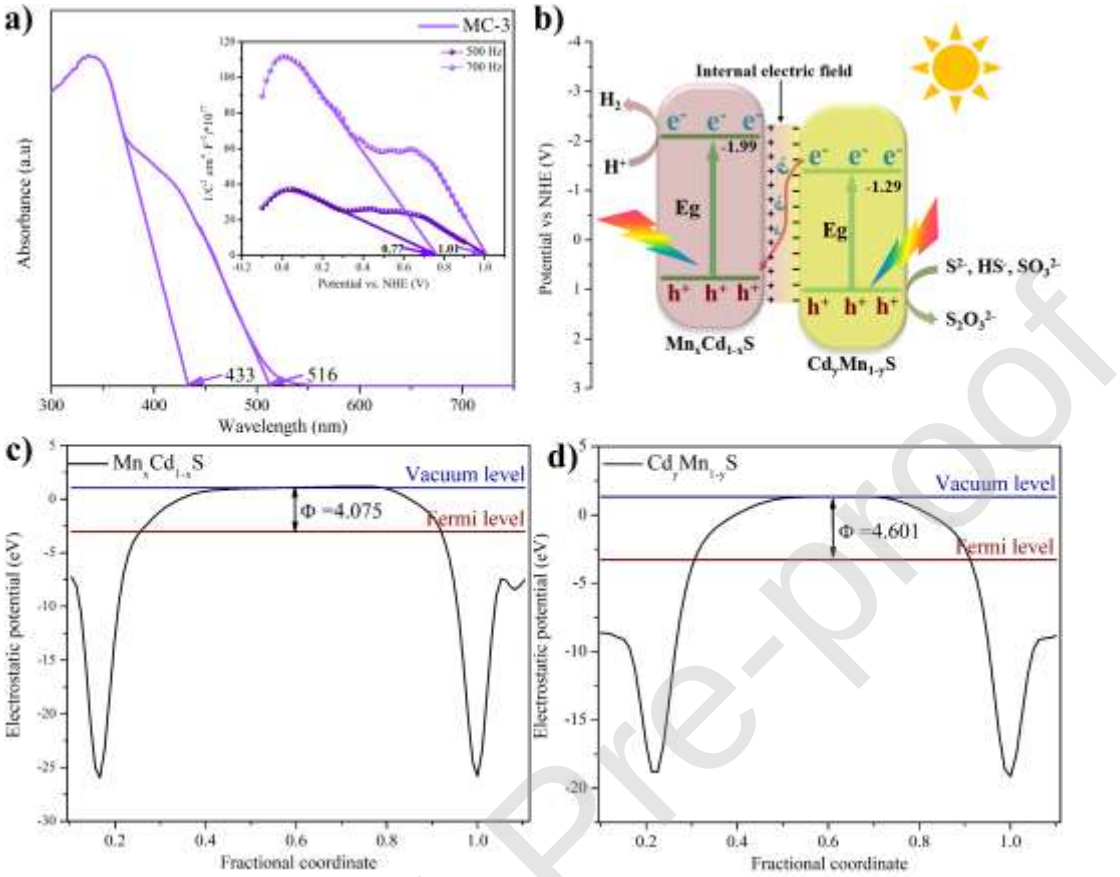

Fig. 4. a) UV–vis DRS of the MC-3 sample (inset is the corresponding MS plots), Work functions of b) $Mn_xCd_{1-x}S$, c) $Cd_yMn_{1-y}S$, d) Schematic illustration of the overall H_2S splitting process.

3.4 Photocatalytic performance enhancement mechanism

Furthermore, the dual-solid-solution heterostructure is demonstrated to maximize the synergy effects of light absorption, spatial charge separation and surface reaction dynamics on the robust H_2S splitting activity. First, all the MC samples exhibit remarkable visible-light response due to the formation of solid solutions (**Fig. 5a**). Even more intriguingly, the UV-Vis DRS profile of the MC-3 composite presents a dual

absorption edge, which is apparently different from naked MnS and CdS, further confirming the formation of $Mn_xCd_{1-x}S$ and $Cd_yMn_{1-y}S$. The charge carrier separation efficiency after photoexcitation was examined by surface photovoltage (SPV) test. As shown in **Fig. 5b**, all the MC samples exhibit an enhanced SPV response as compared to the pristine MnS and CdS, among which MC-3 exhibits the highest SPV response. Indeed, the SPV response intensity is in line with the photocatalytic activity. In addition, the carrier density (N_d) can also be calculated from the Mott-Schottky plots (**Fig. 4a** and **Fig. S9**) using the following Eq. 8.[51]

$$N_d = \frac{2}{e\varepsilon\varepsilon_0} \times \left[\frac{d\left[\frac{1}{C^2}\right]}{dV_s} \right] \quad (8)$$

where e is the electron charge and equal to 1.6×10^{-19} C, C is the space charge capacitance, ε is the dielectric constant of MnS (5.04) [52] and CdS (8.90) [53], the vacuum permittivity of ε_0 is 8.854×10^{-14} F cm^{-1}, and V is the applied potential on the photoanode. The calculated N_d of MnS, CdS and MC-3 are determined to be 4.26×10^7, 1.77×10^7 and 2.79×10^8 (**Table S4**), respectively. The high carrier density of MC-3 represents the efficient carrier separation and transfer property, which again implies that the formation of "Dual-Solid-Solution" heterostructure is in favor of charge carrier transfer and separation. Additionally, the proton reduction activity is investigated by Linear sweep voltammetry (LSV) (**Fig. 5c**), which is also in good agreement with the photocatalytic H_2 production performance. These results show that the proton reduction ability can be significantly improved through the formation of MC hybrids. The contact angle analysis in **Fig. S10** denoted that the contact angle of MC-3 (18.9°) was obviously

smaller than that of the MnS (130.3°) and CdS (32.1°), which is favorable for capturing H^+. The DFT calculations suggest that the existence of the SO_3^{2-} can promote the desorption of S elements from the $Cd_yMn_{1-y}S$ surface by forming $S_2O_3^{2-}$ due to the positive adsorption energy (E_{ads}) of $S_2O_3^{2-}$ (0.63 eV) on the $Cd_yMn_{1-y}S$-S surface (**Fig. 5d**). This result also provides a theoretical evidence endorsing the product-targeting strategy to act as an inspiring approach to ultimately convert both H_2S and Na_2S/Na_2SO_3 sacrificial reagents into the value-added $Na_2S_2O_3$.

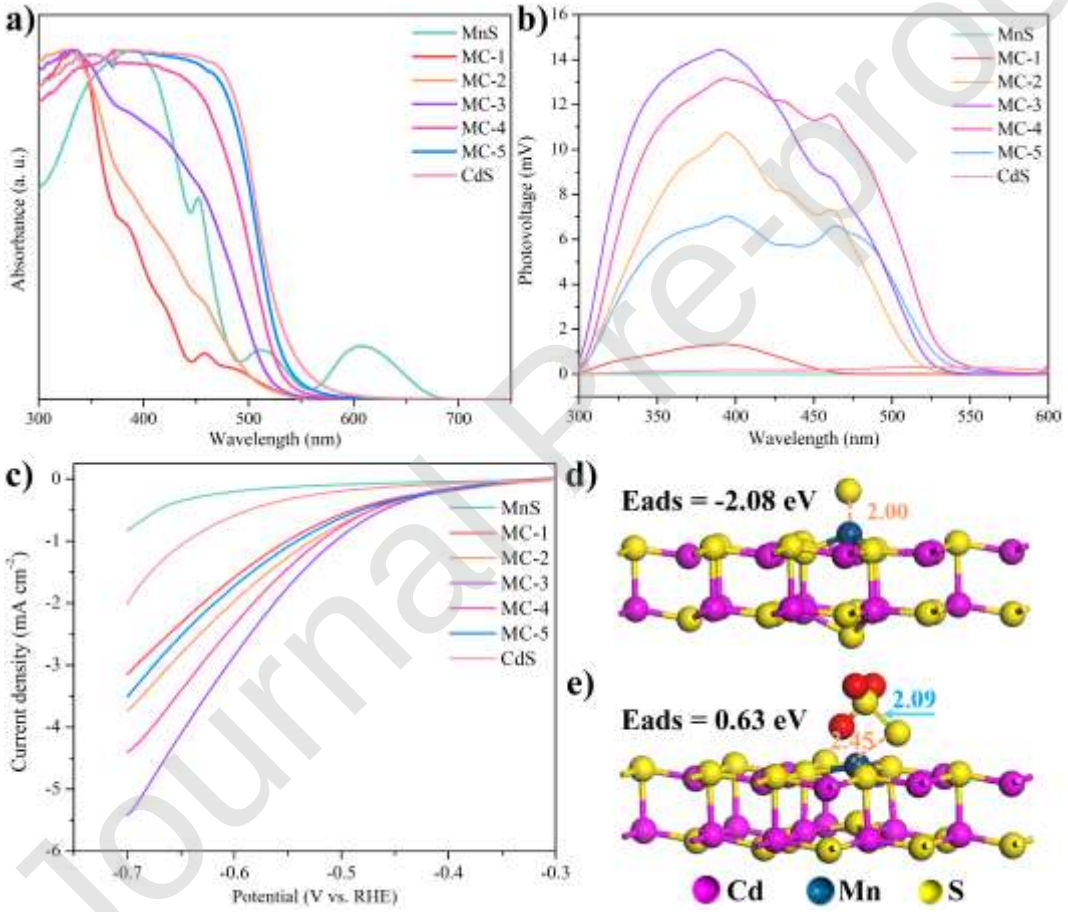

Fig. 5. a) UV–vis DRS, b) SPV spectrum, c) LSV curves of all the samples; The structures of d) S adsorbed on the surface of $Cd_yMn_{1-y}S$, e) SO_3^{2-}adsorbed on the surface of $Cd_yMn_{1-y}S$-S.

On the basis of the above analysis, it is highly expected that the HIPT strategy can

offer great potential for the conversion of Na_2S/Na_2SO_3 into value-added chemicals coupled with state-of-the-art H_2 evolution efficiency via overall H_2S splitting. As portrayed in **Scheme 1**, the synergy effect of Na_2S/Na_2SO_3 and H_2S is essential for the whole process. First, the Na_2S/Na_2SO_3 serves as electron donor to promote the H_2S conversion. In the meantime, H_2S enables the sole generation of $Na_2S_2O_3$ in terms of inhibiting over-oxidized products production and depleting excessive Na_2SO_3. Finally, the application of robust and durable MC "Dual-Solid-Solution" heterostructure makes the HIPT strategy easily accessible for addressing the superiority in light harvesting-efficiency, charge carriers separation ability and surface reaction dynamics.

Additionally, the Alkali Sulfide Method ($2Na_2S + Na_2CO_3 + 4SO_2 \rightarrow 3Na_2S_2O_3 + CO_2$) and Sodium Sulfite Method ($Na_2SO_3 + S \rightarrow Na_2S_2O_3$ (110 °C)) are two typical methods for preparing sodium thiosulfate crystals in the industrial and laboratory, respectively.[54, 55] Both methods are useful to obtain $Na_2S_2O_3$, but need introducing toxic SO_2 gas and valuable raw material i.e. S as well as additional thermal energy, which is detrimental to the environment and may aggravate the energy crisis. In contrast, the advantages of HIPT method are intuitively seen: (i) It can be driven by abundant solar energy only and avoids providing extra energy and precious crude materials; (ii) It enables the simultaneous production of the green energy (H_2) and the value-added $Na_2S_2O_3$ chemical from the toxic industrial exhaust H_2S gas.

4. Conclusions

In summary, we provided a H_2S-induced product-targeting approach for

simultaneous H_2 evolution and value-added chemicals formation using a "Dual-Solid-Solution" heterostructure. As a result, the as-architectured system exhibited a hydrogen evolution rate of 113 mmol g^{-1} h^{-1} with corresponding AQE of 77% at 440 nm, surpassing most previously reported state-of-the-art photocatalysts. Oxidation process is systematically investigated using FTIR technique in combination with IC and XRD, by which the value-added $Na_2S_2O_3$ with high crystallinity is denoted as the only oxidation product. This work not only opens up a new scenario for solar energy conversion integrating with the source utilization of waste H_2S and Na_2S/Na_2SO_3 sacrificial reagents, but also provides a universal method on the design of high efficiency "Dual-Solid-Solution" heterojunction systems for sun light-driven photocatalytic reaction.

Credit author statement

Meng Dan and **Jianglai Xiang** designed the experiments, carried out the synthesis, characterization, catalysis and wrote the paper. **Jian Yang** conducted some synthesis of the catalysts. **Fan Wu** performed the FTIR test, **Chunqiu Han** measured the IC and SPV. **Yunqian Zhong**, **Kaibo Zheng**, and **Shan Yu** contributed to the investigation. **Ying Zhou** supervised the project and co-wrote the paper. All authors joined the discussion and commented on the manuscript.

Conflict of interest

The authors declare no conflict of interest.

Acknowledgements

We acknowledge the National Natural Science Foundation of China (U1862111), Cheung Kong Scholars Programme of China, Chinese Academic of Science "light of west China" Program, Open Fund of State Key Laboratory of Industrial Vent Gas Reuse (SKLIVGR-SWPU-2020-05), Open Fund (PLN201802 and 201928) of State Key Laboratory of Oil and Gas Reservoir Geology and Exploitation (Southwest Petroleum University), and Graduate Student Scientific Research Innovative Project of SWPU (2019cxzd009) for financial support.

Appendix A. Supporting information

Supplementary data associated with this article can be found in the online version at…

References

[1] J. Barber, *Chem. Soc. Rev.* 38 **(2009)** 185-196.

[2] N. S. Lewis, *Science* 315 **(2007)** 798-801.

[3] P. Tao, G. Ni, C. Song, W. Shang, J. Wu, J. Zhu, G. Chen, T. Deng, *Nat. Energy* 3 **(2018)** 1031-1041.

[4] Y. Wang, H. Shi, K. Cui, L. Zhang, S. Ge, J. Yu, *Appl. Catal. B* 275 **(2020)** 119094.

[5] A. Fujishima, K. Honda, *Nature* 238 **(1972)** 37-38.

[6] N. S. Lewis, *Science* 351 **(2016)** 353-364.

[7] K. He, J. Xie, Z. Q. Liu, N. Li, X. Chen, J. Hu, X. Li, *J. Mater. Chem. A* 6 **(2018)** 13110-13122.

[8] X. B. Chen, L. Liu, P. Y. Yu, S. S. Mao, *Science* 331 **(2011)** 746-750.

[9] F. Yang, Q. Zhang, J. Zhang, L. Zhang, M. Cao, W. L. Dai, *Appl. Catal. B* 278 **(2020)** 119290.

[10] S. Selcuk, A. Selloni, *Nat. Mater.* 15 **(2016)** 1107-1112.

[11] R. K. Chava, J. Y. Do, M. Kang, *J. Mater. Chem. A* 7 **(2019)** 13614-13628.

[12] N. Luo, T. Montini, J. Zhang, P. Fornasiero, E. Fonda, T. Hou, W. Nie, J. Lu, J. Liu, M. Heggen, L. Lin, C. Ma, M. Wang, F. Fan, S. Jin, F. Wang, *Nat. Energy* 4 **(2019)** 575-584.

[13] V. Kumaravel, M. D. Imam, A. Badreldin, R. K. Chava, J. Y. Do, M. Kang, A. Abdel-Wahab, *Catalysts* 9 **(2019)** 276.

[14] L. Ye, Z. Ma, Y. Deng, Y. Ye, W. Li, M. Kou, H. Xie, Z. Xu, Y. Zhou, D. Xia, P. K. Wong, *Appl. Catal. B* 257 **(2019)** 117897.

[15] H. F. Ye, R. Shi, X. Yang, W. F. Fu, Y. Chen, *Appl. Catal. B* 233 **(2018)** 70-79.

[16] B. Xia, Y. Zhang, B. Shi, J. Ran, K. Davey, S. Z. Qiao, *Small Methods* 4 **(2020)** 2000063.

[17] I. Tsuji, H. Kato, H. Kobayashi, A. Kudo, *J. Am. Chem. Soc.* 126 **(2004)**13406-13413.

[18] R. B. Wei, Z. L. Huang, G. H. Gu, Z. Wang, L. Zeng, Y. Chen, Z. Q. Liu, *Appl.*

Catal. B 231 **(2018)** 101-107.

[19] H. Yan, J. Yang, G. Ma, G. Wu, X. Zong, Z. Lei, J. Shi, C. Li, *J. Catal.* 266 **(2009)** 165-168.

[20] Y. Li, B. Sun, H. Lin, Q. Ruan, Y. Geng, J. Liu, H. Wang, Y. Yang, L. Wang, K. C. Tam, *Appl. Catal. B* 267 **(2020)** 118702.

[21] H. Lu, J. Zhao, L. Li, L. Gong, J. Zheng, L. Zhang, Z. Wang, J. Zhang, Z. Zhu, *Energy Environ. Sci.* 4 **(2011)** 3384-3388.

[22] Q. Zhang, R. Li, Z. Li, A. Li, S. Wang, Z. Liang, S. Liao, C. T. Li, *J. Catal.* 337 **(2016)** 36-44.

[23] Z. Qiao, J. Wei, X. Jiang, *Org. Lett.* 16 **(2014)** 1212-1215.

[24] P. J. Sunenshine, R. A. Schwartz, C. K. Janniger, *Int. J. Dermatol.* 37 **(1998)** 648-655.

[25] L. Strazzula, S. U. Nigwekar, D. Steele, W. Tsiaras, M. Sise, S. Bis, G. P. Smith, D. Kroshinsky, *JAMA Dermatology* 149 **(2013)** 946-949.

[26] J. Schneider, D. W. Bahnemann, *J. Phys. Chem. Lett.* 4 **(2013)** 3479-3484.

[27] L. Mao, X. Cai, S. Yang, K. Han, J. Zhang, *Appl. Catal. B* 242 **(2019)** 441-448.

[28] M. Dan, S. Yu, Y. Li, S. Wei, J. Xiang, Y. Zhou, *J. Photoch. Photobio. C* 42 **(2020)** 100339.

[29] K. Vikrant, K. H. Kim, A. Deep, *Appl. Catal. B* 259 **(2019)** 118025.

[30] G. Ma, H. Yan, J. Shi, X. Zong, Z. Lei, C. Li, *J. Catal.* 260 **(2008)** 134-140.

[31] J. Reber, F. K. Meier, *J. Phys. Chem.* 88 **(1984)** 5903-5913.

[32] J. F. Reber, K. J. Meier, *Phys. Chem.* 90 **(1986)** 824-834.

[33] M. Dan, S. Wei, D. E. Doronkin, Y. Li, Z. Zhao, S. Yu, J.-D. Grunwaldt, Y. Lin, Y. Zhou, *Appl. Catal. B* 243 **(2019)** 790-800.

[34] M. Dan, Q. Zhang, S. Yu, A. Prakash, Y. Lin, Y. Zhou, *Appl. Catal. B* 217 **(2017)** 530-539.

[35] J. P. Perdew, K. Burke, M. Ernzerhof, *Phys. Rev. Lett.* 77 **(1996)** 3865–3868.

[36] M. D. Segall, P. J. D. Lindan, M. J. Probert, C. J. Pickard, P. J. Hasnip, S. J. Clark, M. C. Payne, *J. Phys-Condens. Mat.* 14 **(2002)** 2717-2744.

[37] M. Lashgaria, M. Ghanimatia, *Chem. Eng. J.* 358 **(2019)** 153-159.

[38] B. B. Kale, J. O. Baeg, S. M. Lee, H. Chang, S. J. Moon, C. W. Lee, *Adv. Funct. Mater.* 16 **(2006)** 1349-1354.

[39] J. S. Jang, H. G. Kim, P. H. Borse, J. S. Lee, *Int. J. Hydrogen Energy* 32 **(2007)** 4786-4791.

[40] J. Yota, V. A. Burrows, *J. Vac. Sci. Technol. A* 11 **(1993)** 1083-1088.

[41] I. V. Pekov, N. V. Chukanov, S. N. Britvin, Y. K. Kabalov, J. Göttlicher, V. O. Yapaskurt, A. E. Zadov, S. V. Krivovichev, W. Schüller, B. Ternes, *Mineral. Mag.* 76 **(2012)** 1133-1152.

[42] S. M. Chen, S. W. Chiu, *Electrochim. Acta* 45 **(2000)** 4399-4408.

[43] R. Chen, Z. H. Yan, X. J. Kong, L. S. Long, L. S. Zheng, *Angew. Chem. Int. Ed.* 57 **(2018)** 16796-16800.

[44] S. Sarkar, S. Sampath, *Chem. Commun.* 50 **(2014)** 7359-7362.

[45] Y. Zhang, Y. Zhao, T. Otroshchenko, A. Perechodjuk, V. A. Kondratenko, S. Bartling, U. Rodemerck, D. Linke, H. Jiao, G. Jiang, E. V. Kondratenko, *ACS Catal.* 10

(2020) 6377-6388

[46] S. Wang, B. Y. Guan, X. Wang, X. W. D. Lou, *J. Am. Chem. Soc.* 140 **(2018)** 15145-15148.

[47] Z. Wang, L. Zhang, T. U. Schülli, Y. Bai, S. A. Monny, A. Du, L. Wang, *Angew. Chem. Int. Ed.* 58 **(2019)** 17604-17609.

[48] Z. Zeng, Y. Yan, J. Chen, P. Zan, Q. Tian, P. Chen, *Adv. Funct. Mater.* 29 **(2019)** 1806500.

[49] X. Yan, Z. Y. Wu, C. Y. Huang, K. L. Liu, W. D. Shi, *Ceram. Int.* 43 **(2017)** 5388-5395.

[50] J. X. Low, B. Z. Dai, T. Tong, C. J. Jiang, J. G. Yu, *Adv. Mater.* 31 **(2018)** 1802981.

[51] Y. Lu, C. Y. Chiang, E. Huang, *Appl. Mater. Today* 20 (**2020**) 100707.

[52] P. Tiwari, J. Jaiswal, R. Chandra, *J. Appl. Phys.* 126 **(2019**) 213108.

[53] I. Vamvasakis, I. T. Papadas, T. Tzanoudakis, C. Drivas, S. A. Choulis, S. Kennou, G. S. Armatas, *ACS Catal.* 8 (**2018**) 8726-8738.

[54] A. F. Holleman, E. Wiberg, N. Wiberg, *Inorganic Chemistry*, Academic Press, San Diego, **2001**.

[55] H. M. Gordin. *Elementary Chemistry*, Vol. 1, Inorganic Chemistry, Medico-Dental Publishing Co, Chicago, **1913**, pp. 162 & 287-288.